Chinese Journal of Chemical Engineering 87 (2025) 157–170

Contents lists available at ScienceDirect

Chinese Journal of Chemical Engineering

journal homepage: www.elsevier.com/locate/CJChE

Full Length Article

Efficient separation of phosphorylated sugars from multi-enzyme system by ultrafiltration and membrane fouling mechanism

Zhengxin Mao [1, 2], Jiachang Shen [1, 2], Mengxin Liu [3], Yanjie Ji [3], Qinhong Wang [4], Maohua Yang [1, *], Jianmin Xing [1, 2, *]

[1] CAS Key Laboratory of Green Process and Engineering, Institute of Process Engineering, Chinese Academy of Sciences, Beijing 100190, China
[2] College of Chemical Engineering, University of Chinese Academy of Sciences, Beijing 100049, China
[3] Tianjin Juno Biotechnology Company, Tianjin 300308, China
[4] CAS, Key Laboratory of Low Carbon Synthetic Engineering Biology, Tianjin Institute of Industrial Biotechnology, Tianjin 300308, China

ARTICLE INFO

Article history:
Received 21 June 2025
Received in revised form
31 July 2025
Accepted 3 August 2025
Available online 20 August 2025

Keywords:
Phosphorylated sugars
Multi-enzyme system
Ultrafiltration
Efficient separation
Membrane fouling

ABSTRACT

Phosphorylated sugars, recognized as central intermediates in carbohydrate metabolism and critical precursors for enzymatic synthesis of rare sugars, face significant technical barriers in their industrial-scale production. The multi-enzymatic preparation systems for these compounds inherently accumulate complex impurities, including protein-based catalysts, residual substrates, and oligosaccharide by-products, posing persistent challenges in product separation and biocatalyst recycling. To address this limitation, we conducted a systematic investigation of ultrafiltration-based separation strategies during the multi-enzyme-catalyzed synthesis of fructose-1,6-bisphosphate (FDP), with particular emphasis on membrane fouling mechanisms. By screening the ultrafiltration membranes, UE020 showed the best performance in the model system, achieving significant separation targets: 99.97% retention of bovine serum albumin, FDP/maltodextrin separation coefficient of 7.41, and FDP recovery of 93.63%. An analysis of the components of resistance revealed that concentration polarization induced by maltodextrin was the main factor constituting the resistance, irreversible resistance due to bovine serum albumin was a secondary effect, and the resistance constituted by FDP was negligible. A mitigation strategy employing powdered activated carbon for dynamic membrane formation significantly improved system performance, reducing irreversible resistance by 59.14% and enhancing flux recovery by 20.85%. In this study, ultrafiltration was strategically employed to achieve efficient separation of FDP and enzyme recovery. Significantly, we deciphered the synergistic fouling mechanisms arising from interactions within the multicomponent system containing phosphorylated sugars, oligosaccharides, and proteins. These findings provide a mechanistic framework for scaling up multi-enzymatic systems dedicated to phosphorylated sugar biosynthesis, effectively bridging the gap between laboratory-scale synthesis and industrial implementation.

1. Introduction

Phosphorylated sugars serve as key intermediate metabolites in glycolysis, contributing to energy metabolism and regulating glycolytic flux. These compounds are utilized across multiple fields, including biomedical research, biochemical analysis, and food industry. Their use in tumor therapy [1,2], glucose metabolism marker research, glycolytic pathway studies [3], and the modulation of the taste and sweetness of foodstuffs are notable examples. Beyond these roles, phosphorylated sugars hold significance in multi-enzyme systems, where they act as intermediates or substrates for downstream reactions. The field of multi-enzyme systems has attracted considerable interest due to its high reaction rate, substrate specificity, adaptable reaction conditions, and high product selectivity [4]. For example, starch and its derivatives can be converted to fructose-6-phosphate *via* a multi-enzyme cascade. Subsequent addition of various enzymes and/or coenzymes enables the production of diverse functional

* Corresponding authors.
E-mail addresses: mhyang@ipe.ac.cn (M. Yang), jmxing@ipe.ac.cn (J. Xing).

https://doi.org/10.1016/j.cjche.2025.08.003

rare sugars [5], such as fructose [6], mannose [7], fructose-1,6-bisphosphate [8], tagatose [9], and allulose [10].

The synthesis of rare sugars by multi-enzyme systems has recently been the focus of numerous research studies [11,12]. Processes such as natural extraction, microbial fermentation or direct chemical synthesis of sugar products have cheap substrates and do not involve enzymatic separation. High yields can often be obtained using conventional separation processes, such as cation exchange chromatography [13], activated carbon adsorption [14], membrane separation [15,16], crystallization and precipitation. Multi-enzyme systems frequently contain target products, multiple enzymes, residual substrates, accumulated intermediates and other associated components. Membrane separation enables stepwise separation of enzymes, substrates, and metabolites from target products, permitting hierarchical recovery and reuse. The process offers high energy efficiency, high separation selectivity, simple operation and low maintenance cost. Fructose-1,6-bisphosphate (FDP) is a derivative of fructose formed by bisphosphorylation, and its structural specificity (C1 and C6 phosphorylation) determines its central position in cellular metabolism. Clinically, FDP treats cardiovascular diseases, neurodegenerative diseases, ischemic diseases, and other clinical disorders [8]. The conventional production process entails the utilization of yeast cells for the purpose of enzymatic conversion [17]. The purification process typically employs a combination of precipitation, ion exchange, and crystallization techniques. Conventional processes frequently cause enzyme/substrate waste and higher production costs. The purification cascade comprises: microfiltration/ultrafiltion (MF/UF) removal of enzymes, oligosaccharides, and macromolecules [18]; Electrodialysis/nanofiltration desalination [19,20]; Ion-exchange resin elimination of neutral impurities [21]; Final concentration/crystallization to obtain high-purity product [22].

Fouling in membrane filtration hinders technological progress, severely reducing separation efficiency and selectivity. During filtration, solutes accumulate on membrane surfaces or penetrate pores, forming filter cakes/gel layers or causing pore blockage. This results in flux decline and elevated transmembrane pressure (TMP). In order to describe the fouling phenomenon, researchers have developed a series of mathematical models, such as series resistance model [23], Hermia model [24], artificial neural network model [25], the extended Derjaguin–Landau–Verwey–Overbeek (XDLVO) model [26], and computational fluid dynamics model [27]. The series resistance model and Hermia model have been extensively utilized to describe fouling phenomena in various membrane separation processes, owing to their high accuracy and excellent alignment with experimental data. The former quantifies resistance distribution, while the latter elucidates membrane fouling mechanisms [28]. Foulant adsorption onto the membrane initiates fouling formation. Subsequently, additional foulants adsorb onto these initial foulants, forming a fouling layer. Thus, foulant-membrane and foulant–foulant interactions are crucial for understanding the fouling mechanism. The XDLVO model quantifies interaction energy as a function of interparticle separation distance. Recently, it has been adopted to describe membrane fouling in numerous studies [29]. In order to alleviate fouling, there have been many studies on the preparation of modified membrane materials and new cleaning strategies. Dynamic membrane (DM) technology mitigates fouling by diverting foulant accumulation to the dynamic layer instead of the base membrane. Powdered activated carbon (PAC) is widely used as a constituent material of DM due to its excellent adsorption properties. Moreover, in practical applications, using PAC as the DM material further enhances the product quality by pre-decolorization.

Optimal membrane candidates were systematically selected using the FDP multi-enzyme catalyzed solution. Performance assessment focused on three key metrics: permeate flux, separation efficiency, and product recovery. Fouling membranes were analyzed through physicochemical characterization (*e.g.*, surface morphology, contact angle) while simultaneously modeling fouling mechanisms *via*: (1) the series resistance model, (2) Hermia model, and (3) XDLVO model. This multi-model approach revealed the cooperative fouling mechanism between phosphorylated sugars, oligosaccharides, and proteins. Building on the identified fouling mechanisms, we will employe dynamic membranes mitigating fouling.

2. Materials and Methods

2.1. Materials

Commercial UF membranes with different molecular weight cut-offs (MWCO) UE010, UE020, UE050 and US020 (relevant parameters are shown in Table 1) were purchased from Rising Sun Membrane Technology (Beijing) CO., Ltd., China. D-Fructose 1,6-bisphosphate trisodium salt octahydrate (98%), bovine serum albumin (96%, BSA) and polyethylene glycol (PEG, molecular weights of 1, 2, 4, 6, 8, 10, and 20 kDa) were purchased from Shanghai Aladdin Biochemical Technology Co., China. Maltodextrin (DP 7–11, MW. 1152–1800 Da) was purchased from Dong Xiao Biotechnology Co., China. Pure water used for all solution configurations was obtained from an ultrapure water machine. 2 L of FDP (40 $g \cdot L^{-1}$), MD (30 $g \cdot L^{-1}$) and BSA (5 $g \cdot L^{-1}$) solutions were configured as model solutions. The binary system contained FDP and MD, and the ternary system contained FDP, MD and BSA.

2.2. UF experiment

The experimental set-up was a homemade device as shown in Fig. 1. The effective filtration area of the flat membrane was 7.07×10^{-4} m^2 and each batch of experiments was performed with a new membrane soaked in pure water for 4 h and rinsed several times with pure water before use. Prior to the filtration of the feed solution, the membrane was pre-compressed with pure water at a TMP of 0.3 MPa for 30 min to ensure that the membrane surface structure remained stable during the filtration process. The feed solution is transported to the cross-flow filtration membrane cell (Hangzhou Super filtration Membrane Technology Co., Ltd., China) *via* a diaphragm pump (Shanghai Xinxishan Industry Co., Ltd., China), and TMP and cross-flow velocity are regulated by bypass throttle valves and flow meter control valves. Driven by the TMP difference, part of the feed solution flows back to the stock tank and the other part passes through the UF membrane to the permeate tank. The mass of the permeate is measured by an electronic balance and the data measured by the balance is transferred to the computer software (iWeight), which records the change in permeate mass over time. Every 10 min the permeate is returned to the feed solution tank to ensure that the feed solution concentration remains stable. Unless otherwise stated, operating

Table 1
Parameters related to UF membranes (data from manufacturer).

Type	Material	MWCO/kDa	Water flux/$L \cdot m^{-2} \cdot h^{-1}$ (25 °C, 0.35 MPa)
UE010	Polyethersulfone (PES)	10	150
UE020	PES	20	200
UE050	PES	50	250
US020	Polysulfon	20	280

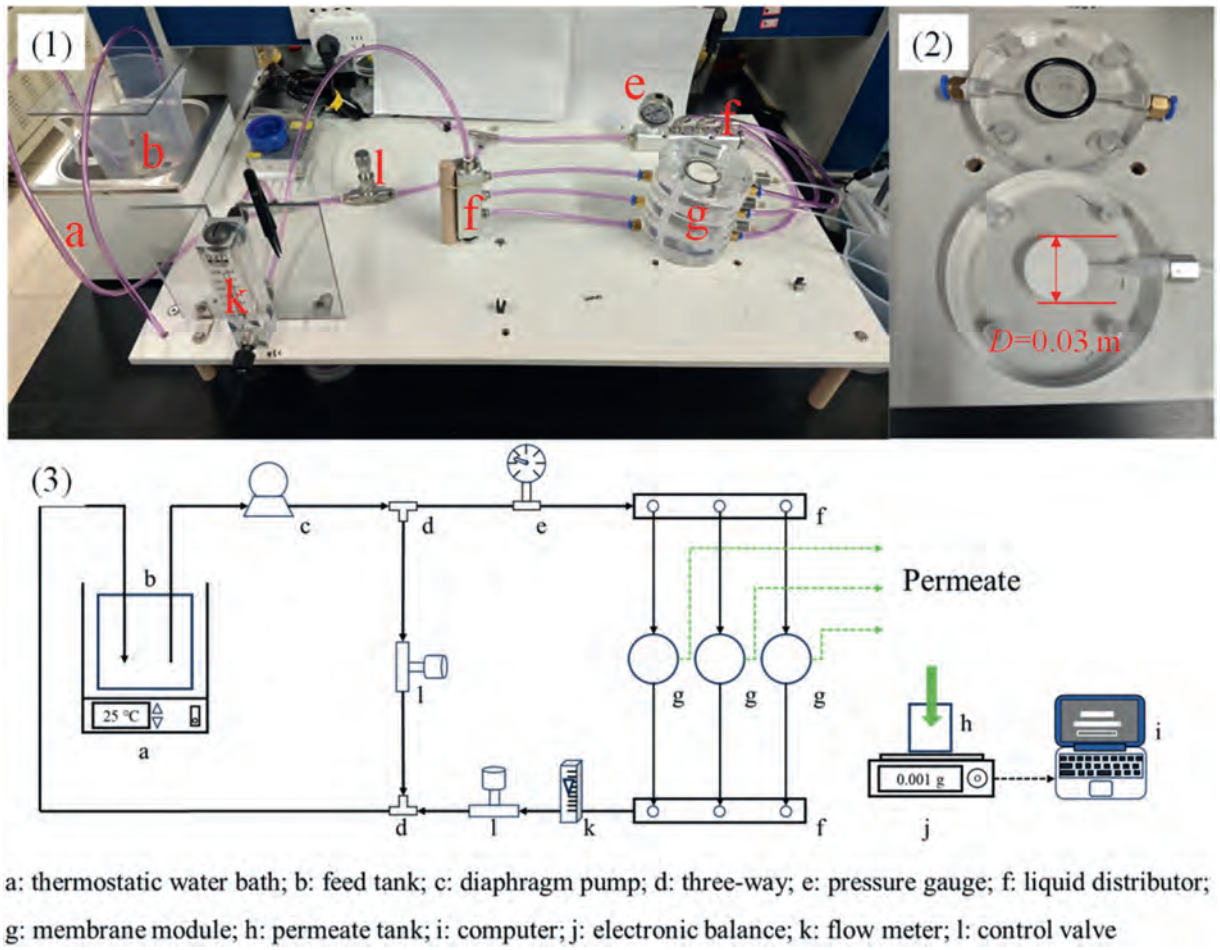

Fig. 1. Device diagram of cross-flow filtration: (1) device picture including membrane modules and flow systems, (2) detailed schematic diagram of membrane module, (3) schematic diagram of ultrafiltration device.

conditions were as follows: TMP 0.1 MPa, cross-flow velocity 1.19 $m \cdot s^{-1}$, control temperature 25°C ± 0.2 °C.

We employed PAC as a foulant mitigation agent to alleviate fouling during ultrafiltration. An *in situ* deposition method was applied to form a dynamic layer, specifically by dosing the raw feed solution with 0.2 $g \cdot L^{-1}$ of PAC powder (400 mesh size; particle size <37 μm) prior to the UF process. The mitigation effectiveness was characterized through resistance analysis and flux recovery evaluation.

2.3. Methods for measuring concentration

The concentrations of FDP and MD were determined by high performance liquid chromatography (HPLC, 1200, Agilent, USA). Chromatographic conditions were as follows: Sugar Pak I column (300 mm × 6.5 mm, 10 μm); pure water as the mobile phase, differential refractive index detector, column temperature of 70 °C, volumetric flow rate of 0.4 $ml \cdot min^{-1}$, injection volume of 10 μl, run time of 10 min.

The concentration of BSA was determined according to the Bradford method [30]. Table 2 shows the standard curves.

2.4. Data process

In the UF experiments, the starting solution was collected at the beginning and the permeate was collected at the end of filtration,

Table 2
Standard curves.

	Equation	Concentration range/$g \cdot L^{-1}$	Correlation coefficient
FDP	$y = 252628x+2889.4$	0.05–0.3	0.9997
MD	$y = 146679x-1291.2$	0.05–0.3	0.9956
BSA	$y = 0.6256x+0.2971$	0.05–0.5	0.9955

and the retention of FDP, MD and BSA by the UF membrane was calculated using the following equation:

$$R = \left(1 - \frac{C_{p,i}}{C_{f,i}}\right) \times 100\% \quad (1)$$

where $C_{f,i}$ and $C_{p,i}$ are the concentrations of feed and permeate, $g \cdot L^{-1}$, respectively; R is retention. The separation factor indicates the selectivity of the membrane for different solutes and is given by the following equation:

$$\alpha = \frac{1 - R_1}{1 - R_2} \quad (2)$$

where α is the separation factor; R_1 is the membrane retention rate of small molecule solute, %; R_2 is the membrane retention rate of large molecule solute, %. If $\alpha = 1$, it means that the retention rate of the two solutes is the same, and the membrane has no separation

effect on the two solutes; if $\alpha > 1$, it means that the membrane has some separation effect on the two solutes, and the larger α is, the better the separation effect is.

Pore size distributions of pristine and fouling membrane were determined using the methods [31,32] described.

2.5. Characterization of foulant and fouling membrane

Zeta potential and mean particle size of FDP, MD and BSA were determined using a nanoparticle size potentiometer (Zetasizer Nano 90, Malvern, UK), respectively. The morphological characteristics of the membrane surface were observed using a scanning electron microscope (SEM, S4800, Hitachi, Japan). The membrane surface was observed using an atomic force microscope (AFM, MultiMode 8, Bruker, Germany) and the roughness was calculated by NanoScope Analysis 1.8. The contact angle of the membrane was determined using a contact angle meter (DSAHT17C, Kruss, Germany). The viscosity of the solution was determined using a viscosity densitometer (DMA5000M-Lovis2000ME, Anton Paar, Austria). The concentration of PEG was measured using a total organic carbon analyzer (TOC-V CPH, Shimadzu, Japan). The molecular weight distribution of MD was determined using gel permeation chromatography (GPC-20A, Shimadzu). Each sample was measured at least three times.

2.6. Fouling model

2.6.1. Series resistance model

The series resistance model is an expression based on Darcy's law which is used to describe the change in permeate flux during the filtration process and at any time during the filtration process the permeate flux can be expressed by the following equation:

$$J = \frac{\Delta P}{\mu \cdot R_t} \tag{3}$$

where J is the permeate flux, $L \cdot m^{-2} \cdot h^{-1}$; ΔP is TMP, Pa; μ is the viscosity of the solution, Pa·s; and R_t is the total resistance, m^{-1}. The total resistance consists of the following components:

$$R_t = R_m + R_{re} + R_{ir} \tag{4}$$

where R_m is intrinsic membrane resistance, m^{-1}; R_{re} is reversible resistance, m^{-1}; R_{ir} is irreversible resistance, m^{-1}.

The fouling resistance component is calculated as follows: R_m can be calculated by determining the pure water flux before filtration in each experiment, R_t can be calculated by determining the flux of the model solution when the filtration process reaches the steady stage, and R_{ir} can be calculated by determining the pure water flux after cleaning the membrane when the filtration is completed.

2.6.2. Hermia model

Hermia proposed a universal classical model to describe the relationship between the permeate flux and filtration time in constant pressure dead-end filtration. The general formula is:

$$\frac{dJ}{dt} = -KJ^{2-n} \times J \tag{5}$$

where t is the filtration time, h; K is the blocking constant; the change in the value of n indicates different forms of fouling, from which four fouling mechanism models are proposed (shown in Table 3): complete blocking model (CBM, $n = 2$), standard blocking model (SBM, $n = 1.5$), intermediate blocking model (IBM, $n = 1$) and cake formation model (CFM, $n = 0$). CBM assumes that the foulant particles completely block the membrane pores, there is no particle accumulation and the fluid cannot pass through the membrane pores; this fouling is usually due to the foulant particle diameter being similar to or slightly larger than the membrane pore diameter. SBM states that the foulant particle diameter is smaller than the membrane pore diameter, the foulant enters the membrane pore and gradually accumulates, reducing the effective membrane pore diameter and increasing the filtration resistance. The formation of this fouling is usually the result of a few medium-sized particles adsorbing and accumulating in the membrane pores. CFM considers that the foulants cover the membrane surface to form a gel/cake layer and the formation and thickening of the cake layer increases the filtration resistance and leads to a reduction in permeate flux. This type of fouling occurs in most filtration processes. IBM is a form of fouling between CBM and CFM where there is both membrane pore blockage and cake formation, which together result in increased resistance. A schematic of the model blockage is shown in Fig. 2.

The classical model is available for dead-end filtration under constant pressure conditions, but the continued use of the classical model introduces a large deviation in cross-flow filtration due to the presence of a non-negligible tangential flow. Therefore, the steady state flux (J_{ss}, $L \cdot m^{-2} \cdot h^{-1}$) was introduced to correct the classical model and the mass transfer model was obtained with the following general formula:

$$\frac{dJ}{dt} = -KJ^{2-n}(J - J_{ss}) \tag{6}$$

2.6.3. XDLVO model

The XDLVO model asserts that the total interfacial energy (ΔG^{TOT}, $mJ \cdot m^{-2}$) between the solute and the membrane surface consists of the acid-base interaction energy (ΔG^{AB}, $mJ \cdot m^{-2}$), van der Waals interaction energy (ΔG^{LW}, $mJ \cdot m^{-2}$), and electrostatic double layer interaction energy (ΔG^{EL}, $mJ \cdot m^{-2}$), which is given in Eq. (11):

$$\Delta G^{TOT} = \Delta G^{AB} + \Delta G^{LW} + \Delta G^{EL} \tag{11}$$

When the total interfacial energy is positive, the two substances repel each other; when the total interaction energy is negative, the two substances attract each other. The interfacial interaction energy is a function of the interaction distance h (m) and is calculated as follows:

$$\Delta G^{AB}(h) = 2\pi r \Delta G^{AB}_{h_0} \exp\left(\frac{h_0 - h}{\lambda}\right) \tag{12}$$

$$\Delta G^{LW}(h) = 2\pi r \Delta G^{LW}_{h_0} \frac{{h_0}^2}{h} \tag{13}$$

$$\Delta G^{EL}(h) = \pi \varepsilon_0 \varepsilon_r r \left[2\xi_m \xi_f \ln\left(\frac{1 + e^{-\kappa h}}{1 - e^{-\kappa h}}\right) + \left({\xi_m}^2 + {\xi_f}^2\right) \ln\left(1 - e^{-2\kappa h}\right) \right] \tag{14}$$

Table 3
Mass transfer expression for the Hermia model.

Model	n	Mathematical equation	Code
CBM	2	$dJ/dt = -K_a(J - J_{ss})$	(7)
SBM	1.5	$dJ/dt = -K_b(J - J_{ss})J^{0.5}$	(8)
IBM	1	$dJ/dt = -K_c(J - J_{ss})J$	(9)
CFM	0	$dJ/dt = -K_d(J - J_{ss})J^2$	(10)

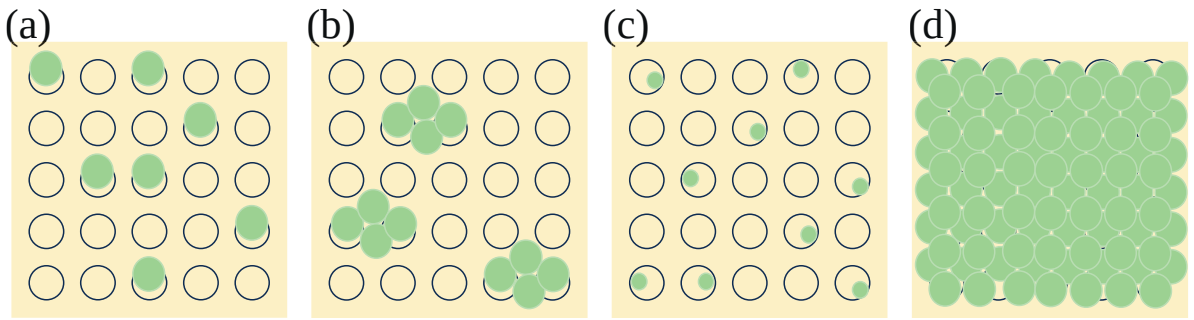

Fig. 2. Schematic diagrams of the Hermia model: (a) CBM, (b) IBM, (c) SBM, (d) CFM.

where r is the radius of solute particles, nm; λ is the decay length of the polar force in water, which takes the value of 0.6 nm; ε_0 is the vacuum permittivity, 8.85 × 10^{-12} F·m^{-1}; ε_r is the relative permittivity of aqueous solution, which takes the value of 81; ξ_m and ξ_f are the values of zeta potentials of the membrane surface and the foulants, mV, respectively; κ is the reciprocal of the Debye shielding constant, which takes the value of 0.104 nm^{-1}. The cohesive free energy (ΔG^{sis}) of the substance can be calculated when its molecules are in contact in an aqueous solution. $\Delta G^{AB}_{h_0}$, $\Delta G^{LW}_{h_0}$ and $\Delta G^{EL}_{h_0}$ are the interfacial interaction energies when the interaction distance between the two substances is the minimum ($h_0 = 0.158$ nm), mJ·m^{-2}; and the calculation formula is as follows:

$$\Delta G^{AB}_{h_0} = 2\left(\gamma_l^+\right)^{0.5}\left[\left(\gamma_m^-\right)^{0.5} + \left(\gamma_f^-\right)^{0.5} - \left(\gamma_l^-\right)^{0.5}\right] + 2\left(\gamma_l^-\right)^{0.5}\left[\left(\gamma_m^+\right)^{0.5} + \left(\gamma_f^+\right)^{0.5} - \left(\gamma_l^+\right)^{0.5}\right] - 2\left[\left(\gamma_m^+\gamma_f^-\right)^{0.5} + \left(\gamma_f^+\gamma_m^-\right)^{0.5}\right] \tag{15}$$

$$\Delta G^{LW}_{h_0} = 2\left(\gamma_l^{LW} - \gamma_m^{LW}\right)^{0.5}\left(\gamma_f^{LW} - \gamma_l^{LW}\right)^{0.5} \tag{16}$$

$$\Delta G^{EL}_{h_0} = \frac{\varepsilon_0\varepsilon_r\kappa}{2}\left(\xi_m{}^2 + \xi_f{}^2\right)\left[1 - \coth(\kappa h) + \frac{2\xi_m\xi_f}{\xi_m{}^2\xi_f{}^2}\operatorname{csch}(\kappa h)\right] \tag{17}$$

where the subscripts m, l and f denote the membrane, solution and pollutant, respectively; where γ^+, γ^-, γ^{LW} and γ^{AB} denote the electron acceptor parameter, the electron donor parameter, the nonpolar property parameter and the polar property parameter of the corresponding substances, respectively. By determining the contact angle of the liquid on the membrane surface with the known surface tension parameter and combining with Young's Eqs. (18)–(20), the surface tension components of the membrane can be calculated.

$$\gamma^{TOT} = \gamma^{LW} + \gamma^{AB} \tag{18}$$

$$\gamma^{AB} = 2(\gamma^+\gamma^-)^{0.5} \tag{19}$$

$$0.5\gamma_l^{TOT}(1 + \cos\theta) = \left(\gamma_l^{LW}\gamma_s^{LW}\right)^{0.5} + \left(\gamma_l^+\gamma_s^-\right)^{0.5} + \left(\gamma_l^-\gamma_s^+\right)^{0.5} \tag{20}$$

where γ_l^+, γ_l^- and γ_l^{LW} are the surface tension parameters of the probe liquid, mJ·m^{-2}; γ_s^+, γ_s^- and γ_s^{LW} are the surface tension parameters of the pollutant or membrane, mJ·m^{-2}; θ is the contact angle, (°).

3. Result and Discussion

3.1. Efficient separation of FDP

3.1.1. Selection of TMP

UE010, UE020, UE050 and US020 were selected for UF of the ternary model solution. By keeping the cross-flow velocity constant (1.19 m·s^{-1}), the variation of permeate flux with TMP was analyzed to determine the appropriate operating conditions. In 1995, Field *et al.* [33] first introduced the concept of 'critical flux', which is important to minimize irreversible fouling on the membrane surface while maintaining a high flux. The critical flux is the irreversible fouling threshold below which only reversible fouling occurs and above which irreversible fouling begins to occur [34,35]. The limiting flux is the maximum flux that can be achieved as the TMP increases. Using the ternary system as a reference, the flux change results are shown in Fig. 3 when TMP increase from 0.1 MPa to 0.4 MPa. The relationship between TMP, solution osmotic pressure and osmotic flux follows the transport equation [11]:

$$J = L_p(\mathrm{TMP} - \sigma\Delta\pi) \tag{21}$$

$$\Delta\pi = \Delta c_i RT \tag{22}$$

where L_p is the pure water permeability coefficient (Table 4); σ is the reflection coefficient; $\Delta\pi$ is the osmotic pressure; σ [0,1] indicates the retention capacity of the membrane for solutes. The larger σ is, the higher the retention rate is, and when $\sigma = 1$, it indicates complete retention; Δc_i is the concentration difference between the two sides of the membrane.

Under conditions of constant solution composition and TMP, solute flux is governed exclusively by membrane permeability and the reflection coefficient. Consistent with the Donnan-steric pore model with dielectric exclusion [36], solute retention increases with flux until a critical flux threshold is attained. Beyond this threshold, retention plateaus, exhibiting no further increase. Meanwhile, the reflection coefficient stabilizes, thereby maintaining a constant solute flux. No critical pressure point was observed in Fig. 3 between 0.1 and 0.4 MPa, indicating a membrane critical pressure below 0.1 MPa, probably resulting from the system's high solute concentration. Under lower pressures, solutes adsorb rapidly onto the membrane surface, blocking pores and

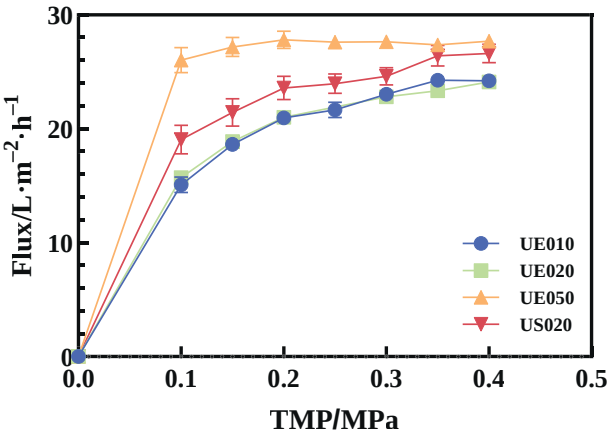

Fig. 3. Trends in permeate flux with TMP.

leading to immediate irreversible fouling. Increasing TMP results in a slow flux rise and further accumulation of irreversible fouling until the limiting pressure is reached, at which point permeate flux stabilizes. Limiting pressure of UE010, UE020, UE050 and US020 membranes are 0.35, 0.30, 0.20 and 0.35 MPa, respectively, and their limiting fluxes are 24.25, 23.33, 27.80, and 26.41 $L \cdot m^{-2} \cdot h^{-1}$. Once TMP reaches the limiting pressure and increases further, concentration polarization (CP) intensifies. The thickening fouling layer and resulting steep rise in resistance counteract the increasing TMP, leading to flux stabilization. Although higher treatment efficiency is ideally achieved below the critical pressure, irreversible fouling occurs even at 0.1 MPa in this system due to the high solute concentration (70 $g \cdot L^{-1}$ sugar, 5 $g \cdot L^{-1}$ protein). Consequently, an operating TMP range of 0.1—0.2 MPa was selected to ensure practical treatment efficiency.

3.1.2. Selection of UF membranes

Operating conditions: TMP 0.1 MPa, cross-flow velocity 1.19 $m \cdot s^{-1}$. The retention rates of FDP, MD and BSA by the four membranes are shown in Table 5 and Table 6. The changes in permeate fluxes are shown in Fig. 4.

Table 5 and Fig. 4(a) and (b) represent the changes in retention and permeate flux of the binary system UF experiments, respectively. The steady-state fluxes of UE010, UE020, UE050 and US020 were 24.90, 32.10, 39.77 and 39.09 $L\ m^{-2} \cdot h^{-1}$, respectively. From UE010, UE020 to UE050, An increase in the MWCO of the membranes correlated with increased membrane pore size and flux, alongside decreased retention of FDP and MD and a lower separation factor. Compared to US020, the flux of UE020 was lower and the retention rate was higher, which might be due to the better hydrophilicity of polysulfone material. The effect of TMP on the retention rate and flux was investigated for UE020 as an example, as shown in Fig. 4(b). Higher pressure increased flux, but membrane fouling limited its effectiveness: a 0.1 MPa pressure rise improved steady-state flux by merely 12%. Despite polymerization

Table 4
Pure water permeability coefficient ($L \cdot m^{-2} \cdot h^{-1} \cdot MPa^{-1}$).

	UE010	UE020	UE050	US020
L_p	804.0 ± 31.8	1184.7 ± 31.2	2064.3 ± 45.8	2543.9 ± 54.8

Table 5
Retention of binary system.

	UE010	UE020	UE050	US020	UE020①
FDP/%	8.51 ± 0.70	3.83 ± 1.41	1.63 ± 0.17	−2.60 ± 1.25	1.93 ± 1.07
MD/%	72.96 ± 1.07	63.31 ± 1.22	41.33 ± 2.75	44.48 ± 2.82	57.99 ± 0.29
α	3.38	2.62	1.68	1.85	2.33

① TMP is 0.2 MPa, other conditions remain unchanged.

degree (7—11) and molecular weight (1152—1800 Da), Table 5 shows all four membranes retained some MD, with UE010 achieving remarkably high retention (72.96%). This contradicts the primary UF retention mechanism of size sieving, wherein retention implies the solute (MD) is larger than the membrane pores. As to whether intermolecular agglomeration of MD occurs in aqueous solution or its own size is larger, further study is still needed. Therefore, we measured the molecular weight distribution (MWD) of MD solutions with different concentrations, and the results are shown in Fig. 5.

From Fig. 5, we can see that the retention time of the MWD curves of MD were basically the same at concentrations of 5, 20 and 50 $g \cdot L^{-1}$, which indicated that the MWD of MD was independent of its concentration. This means that MD did not undergo intermolecular agglomeration in aqueous solution. In addition, we can find that the MWD of MD has a 'bimodal' shape, with the peaks falling around 2200 and 19700. The ratio of the peak areas of the two peaks is approximately 3:7. This is similar to the MWD of MD from other sources in the literature [37]. The high content (~70%) of high molecular weight polymers (19.70 kDa) is a key factor in the high retention of MD.

Table 6 and Fig. 4(c) and (d) show the changes of the retention rate and permeate flux of the ternary system, respectively. The steady-state fluxes of UE010, UE020, UE050 and US020 were 13.76, 16.67, 25.49 and 24.62 $L \cdot m^{-2} \cdot h^{-1}$, which were consistent with the trend of the binary system. The molecular weight of BSA is about 66 kDa, which is higher than MWCO of the four membranes. Therefore, the retention rate of BSA can reach more than 99.5% for all of them, and it can be considered that all four membranes can achieve good retention of BSA. Furthermore, BSA addition significantly increased the retention of higher-molecular-weight MD, while minimally affecting the retention of smaller FDP. Consequently, the separation factor between FDP and MD improved substantially. However, in the UF experiments of the three-component system, an interesting result appeared: the retention rate of UE020 for FDP and MD was higher than that of UE010, which may be related to the fouling occurring on both membrane surfaces. When the diameter of the pollutant particles is close to the membrane pore diameter, the solutes are more likely to block the membrane pores to form a cake layer, resulting in higher retention rates. Increasing TMP to 0.2 MPa resulted in a 45% increase in steady-state flux. Flux remained relatively stable over the 6-h filtration period, showing no significant decay trend. This

Table 6
Retention of ternary system.

	UE010	UE020	UE050	US020	UE020①
FDP/%	4.59 ± 0.57	6.37 ± 0.62	4.37 ± 0.47	−3.05 ± 0.17	−0.91 ± 0.35
MD/%	83.92 ± 0.67	87.37 ± 0.61	49.34 ± 2.33	41.31 ± 3.89	46.92 ± 2.68
BSA/%	100.05 ± 0.25	99.97 ± 0.13	99.52 ± 0.07	99.73 ± 0.14	99.74 ± 0.10
$\alpha_{F\text{-}M}$	5.93	7.41	1.89	1.76	1.90

① TMP is 0.2 MPa, other conditions remain unchanged.

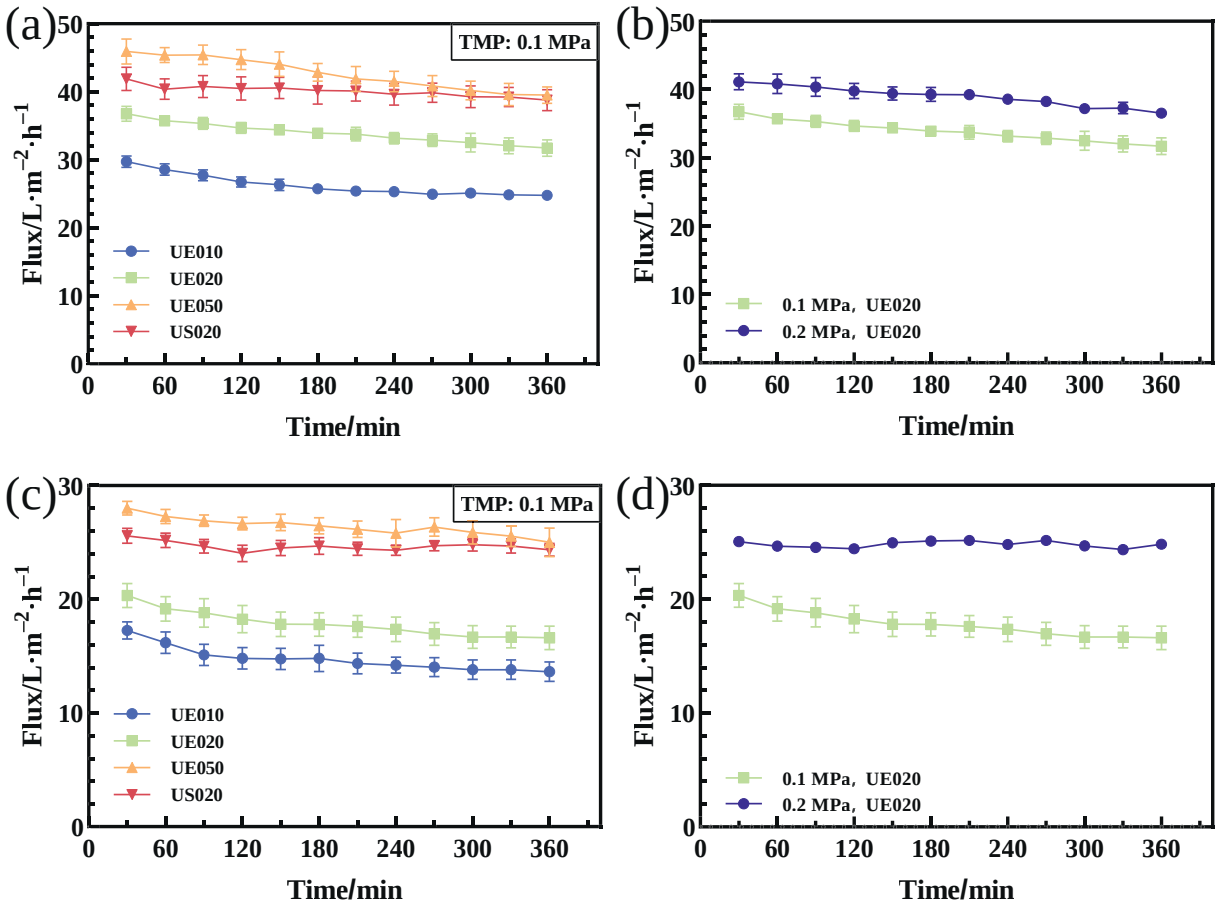

Fig. 4. Flux changes in the binary/ternary system: (a) and (b) FDP/MD system, (c) and (d) FDP/MD/BSA system.

marked difference from the two-component system is likely due to reduced membrane fouling.

3.2. Fouling behavior under the joint control of MD and proteins

3.2.1. Characterization of fouling membrane

Based on separation efficiency and permeate flux performance against the FDP multi-enzyme model solution, UE020 was selected as the primary UF membrane for further investigation. Morphological characterization and pore size distribution analyses were conducted on both pristine and fouling membranes. The fouling samples were prepared by filtering the ternary model solution for 2 h, followed by gentle rinsing and room-temperature vacuum drying overnight. Characterization tests were performed on at least three randomly selected locations per sample. The SEM image, AFM image and pore size distribution of the pristine and fouling membrane are shown in Figs. 6–8, respectively.

SEM characterization of UE020 reveals distinct surface morphology changes following fouling (Fig. 6). While the fouling layer partially covers the membrane surface, substantial effective filtration area remains accessible. Magnified views further indicate: (i) Dark deposits partially occluding membrane pores; (ii) Uniformly sized white particles irregularly distributed across the surface matrix. Crucially, the absence of particle agglomeration and lack of dense gel/cake layer formation indicate minimal fouling occurred. AFM characterization of pristine and fouling membranes (Fig. 7) demonstrates color gradients corresponding to surface topography: lighter regions denote elevated features (membrane peaks or adsorbed particles), while darker areas represent depressions or pores. Height profiles measured at three randomly selected locations revealed ranges of −8.5 to 7 nm (pristine) *versus* −23 to 24 nm (fouling), indicating no statistically significant surface height alteration. Three-dimensional reconstructions confirmed SEM observations, showing sparse particle deposition and minimal roughness change (R_a: 1.46 nm pristine → 2.10 nm fouled). Collectively, these analyses verify: (i) Limited surface coverage by foulants; (ii) Retention of substantial accessible pore networks; (iii) Preservation of solvent transport pathways.

Compared to the dense fouling layers formed by polysaccharides [38] and proteins [39] in other studies, the system under investigation in this study resulted in only minor contamination of the membrane surface. This suggests that the formation of gel/cake layer was not the primary cause of the contamination. Consequently, membrane fouling likely originated from the ingress of small-molecule pollutants (MD or FDP) into the membrane pores and their adsorption onto the pore walls. This process reduces the effective pore size and increases filtration resistance. To quantify this pore size change, the pore size distributions of pristine and fouled membranes were analyzed (Fig. 8). Retention rate experiments using PEG tracers of varying molecular weights were performed. The results showed that MWCO of the pristine UE020 membrane was 22.0 kDa. After fouling, MWCO decreased significantly to 6.6 kDa. Similarly, the average membrane pore size

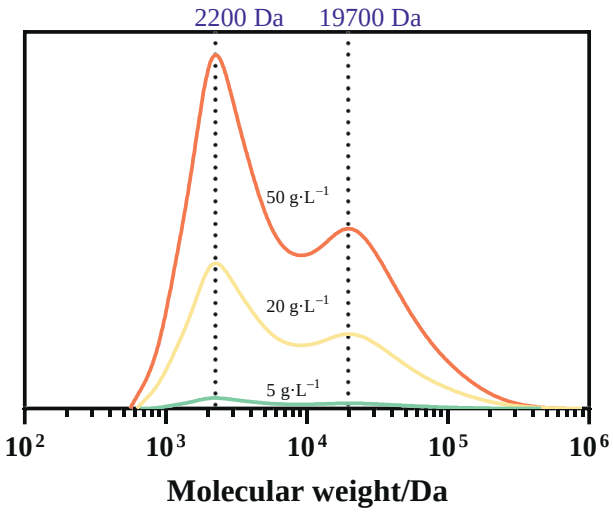

Fig. 5. Molecular weight distribution curves of different concentrations of MD.

declined from 5.89 nm to 2.69 nm. This demonstrates that pollutants entered the membrane pores, adsorbed onto the walls, and accumulated over time, leading to substantial pore constriction.

Preliminary results from SEM, AFM and pore size distribution tests indicate that the formation of fouling is primarily attributable to pore blockage. In the following, the series resistance model and Hermia mass transfer model will be employed to fit the flux data, describe the fouling process and validate the conclusions obtained from the characterization.

3.2.2. Distribution of fouling resistance

Resistance distributions were examined for both the FDP/MD system and the FDP/MD/BSA system. Using the UE020 membrane as an example, resistance distribution was analyzed across different operating pressures (Fig. 9). Across the membrane series (UE010 to UE050), increasing MWCO and pore size correlated with decreasing irreversible resistance and total resistance. Comparing membranes of identical MWCO (UE020 and US020), reversible resistance values were similar. However, US020 exhibited lower irreversible resistance, attributable to the enhanced hydrophilicity of its polysulfone material. This hydrophilic character reduces protein adsorption propensity and consequently decreases fouling layer formation. Irreversible resistance arises primarily from solute adsorption within or blockage of membrane pores. Its magnitude depends on solute-membrane interaction strength and the solute radius-to-pore diameter ratio. Overall, the data reveal a clear trend: larger membrane MWCO corresponds to smaller irreversible resistance [40].

For the FDP/MD binary system, reversible resistance is the main factor constituting the total resistance, accounting for 62%, 72%, 94% and 92%, respectively. The molecular weights of both FDP and MD were lower than that of MWCO of UE020, so further discussion is still needed for the irreversible fouling formed on their membrane surfaces. For the ternary system, the irreversible resistance was significantly increased due to the addition of BSA, which accounted for 46%, 41%, 37%, and 17%, respectively. BSA could not

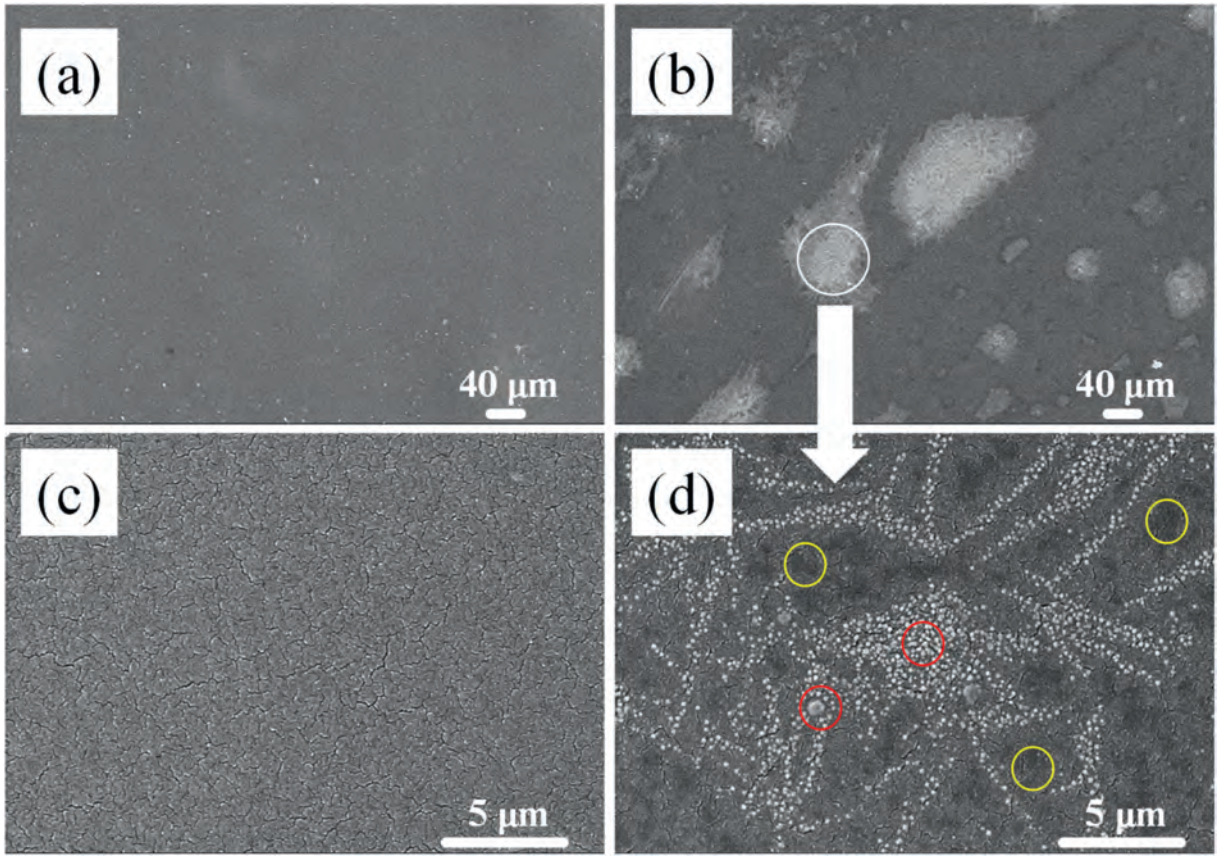

Fig. 6. SEM images of UE020: (a) and (c) pristine membrane, (b) and (d) fouling membrane.

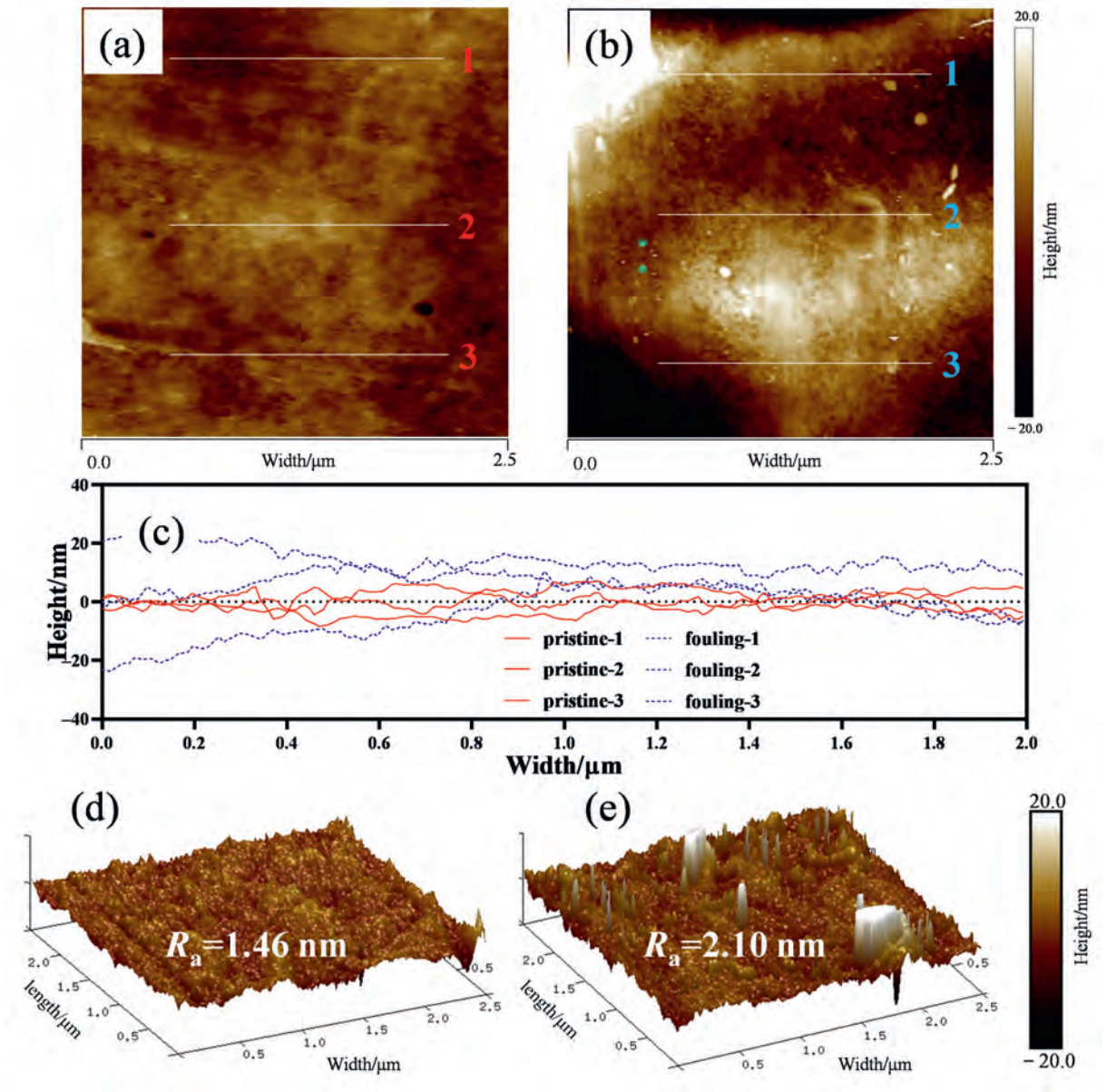

Fig. 7. AFM characterization of UE020: (a) and (c) pristine membrane, (b) and (d) fouling membrane.

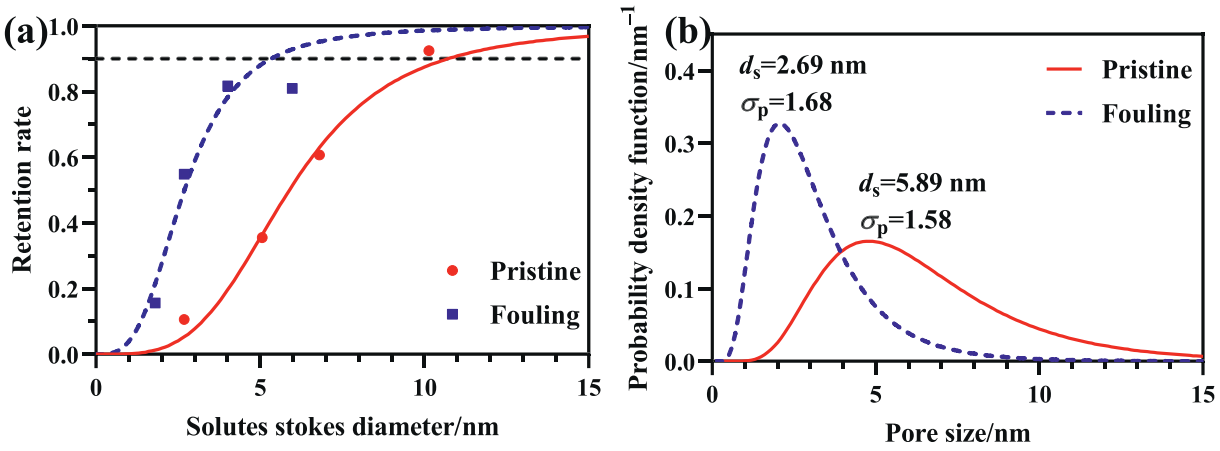

Fig. 8. Retention test of PEG (a) and pore size distribution (b) before and after UE020 fouling.

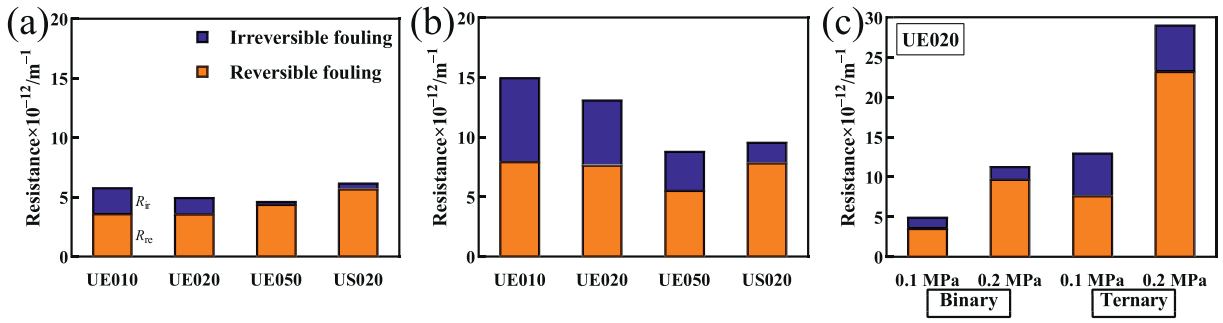

Fig. 9. Resistance distributions of multi-component systems: (a) binary, (b) ternary, (c) different TMP.

pass through the membrane pores due to its hydrophobicity and molecular size, but only adsorbed on the surface of the membrane, and it was difficult to be removed by pure water rinsing. Next, we carried out a study of the fouling process of UE020 on a single component, as shown in Fig. 10.

The three fractions exhibited distinctly different fouling performances. FDP exhibited the lowest total resistance due to its smallest molecular size, but it was found that the percentage of irreversible resistance increased significantly with increasing concentration. We hypothesized that FDP enters the membrane pores and adsorbs onto the pore walls, reducing pore size. This effect may arise from electrostatic interactions. We measured the zeta potential of FDP across a range of pH values (Fig. 11(a)). FDP was found to be electrically neutral near pH 4.4. The flux decline of FDP solutions was subsequently tested at pH 4.5, 6.5, and 9.5 (Fig. 11(b)). The results show essentially identical flux decay patterns across these different pH conditions. This strongly suggests that the fouling behavior of FDP is independent of its surface charge, contradicting an electrostatic fouling mechanism. Additionally, we compared the fouling propensity of neutral sugars (sucrose and maltose) with molecular weights similar to FDP (Fig. 11(c)). The results demonstrate that when the solute molecular weight is significantly below MWCO, membrane fouling becomes independent of solute charge. Instead, fouling is governed solely by molecular size/dimensions, consistent with a size-exclusion mechanism where the solute radius-to-pore diameter ratio dominates. These findings indicate that all three small-molecular-weight sugars induced pore clogging during UF with UE020. The sugars penetrated membrane pores and adsorbed onto the pore walls, thereby reducing the effective pore diameter. The molecular weight of MD showed a bimodal distribution, as shown in Fig. 5, with peaks falling at 2.2 and 19.7 kDa (near to the MWCO), respectively. The MD with low degree of polymerization (DP) passed through the membrane, and the high DP was rejected. A high proportion of reversible fouling was observed during ultrafiltration. Given the absence of significant fouling layers in SEM and AFM analyses, CP is indicated as the primary fouling mechanism for MD. This effect intensified with increasing MD concentration, consistent with CP's dependence on bulk solute concentration. The fouling of BSA is mainly irreversible fouling.

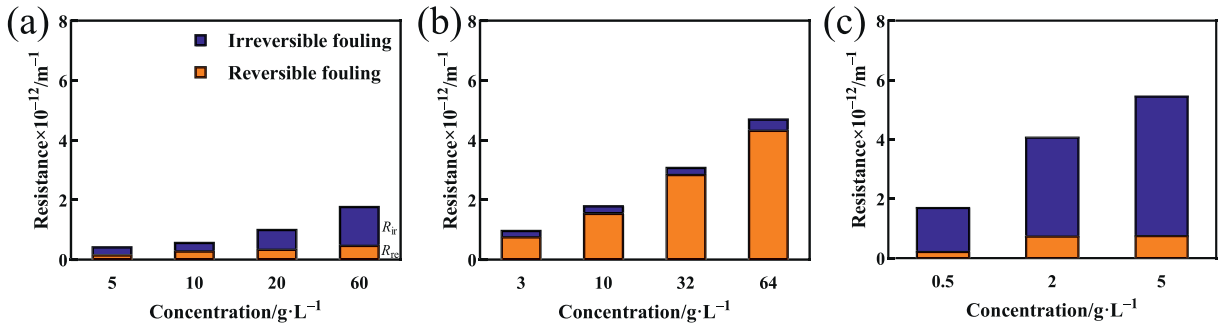

Fig. 10. Resistance distributions of one-component systems: (a) FDP, (b) MD, (c) BSA.

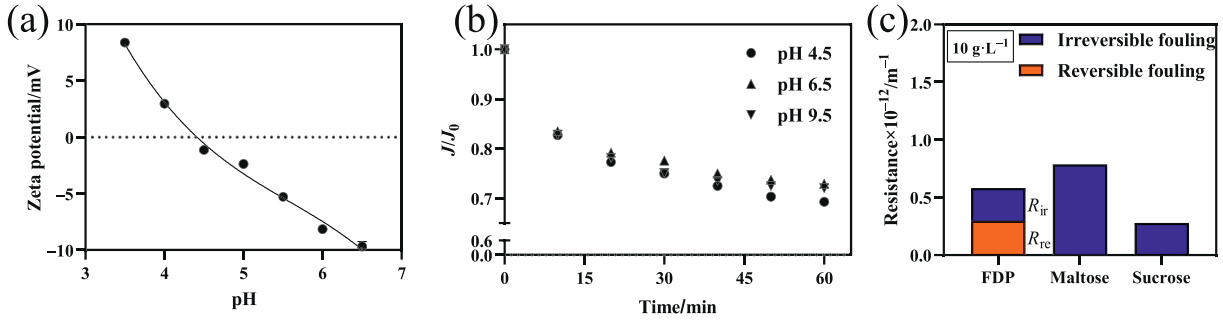

Fig. 11. Impacts of FDP chargeability on fouling behavior: (a) zeta potentials at different pH, (b) normalized fluxes at different pH, (c) resistance distribution of different disaccharides.

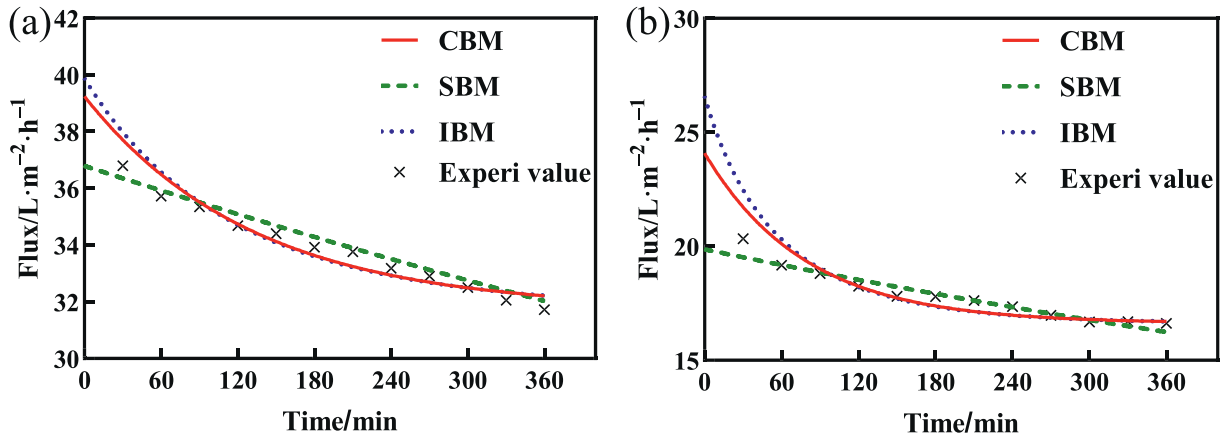

Fig. 12. Fitting results of Hermia mass transfer model for UE020: (a) binary system and (b) ternary system.

There are more studies related to it, so the fouling behavior of BSA will not be discussed in depth.

3.2.3. Analysis of fouling mechanism

To elucidate the effects of membrane materials and feed systems on fouling mechanisms, permeate flux data were fitted using the Hermia mass transfer model. The type of fouling was determined by comparing the correlation coefficients of the fitted regression equations, taking UE020 as an example, as shown in Fig. 12, and other fitting results are shown in Tables 7 and 8. It can be seen that CBM, IBM, and CFM are the main fouling mechanisms for UE010, and all four types of fouling occurring on US020 membranes are present. The most dominant fouling mechanism for UE020 and UE050 is SBM. The correlation coefficient reached more than 0.98. For UE010, large solutes cannot penetrate the pores due to size exclusion. This causes initial pore blockage, followed by solute accumulation that develops into cake formation. As for UE020 and UE050, due to the large pore size, solutes and particles preferentially entered the membrane pores and adsorbed on the pore wall, which reduced the pore size and led to the decrease of permeate flux. The ternary system exhibited similar fitting results as the binary system.

The results of the series resistance model and the Hermia mass transfer model revealed that, MD-induced reversible fouling (concentration difference polarization) is an important factor in the formation of fouling. The effect of irreversible fouling is also more significant for UE020, where a small amount of BSA is deposited on the surface of the membrane, and FDP enters the membrane pores resulting in a reduced pore size.

3.2.4. Interaction between foulant and membrane

Membrane fouling initiates when foulants contact the membrane surface and adsorb, forming an initial layer. Subsequent foulants deposit onto this layer, increasing its thickness and fouling severity. To fundamentally analyze foulant-membrane interactions, interfacial forces must be examined. The XDLVO theory quantifies interaction energies between solid surfaces, making it suitable for modeling foulant–foulant and foulant–membrane interactions—key drivers of fouling. Here, we apply XDLVO theory to evaluate interfacial interactions between the membrane and FDP, MD, BSA, and their ternary mixture, providing mechanistic insights into UE020 fouling behavior. Before modeling, feedstock solution and membrane characteristics were determined (Table 9).

Water contact angles measured 76.68°, 71.49°, and 70.42° for FDP, MD, and BSA, respectively, confirming their hydrophilic nature. Hydrophilicity decreased in the order: BSA > MD > FDP. Additionally, the zeta potential of UE020 was −22.95 mV, and the potentials of all three components were also negative. It can be hypothesized that the effect of electrostatic repulsion between solutes might have some alleviating effect on membrane fouling. Using the surface tension data of three probe liquids and contact angle measurements on fouling membranes, we calculated the interfacial tension parameters of foulants and pristine membranes *via* Eqs. (18)–(20). Results are presented in Table 10.

From the data in Tables 10 and it can be seen that the nonpolar component of the UE020 membrane is 48.78 m·m^{-2}, which is 37.5 times of the polar component (1.30 mJ·m^{-2}), indicating that UE020 is a nonpolar surface. In the polar action energy of pollutants, the electron acceptor tension component (γ^-) is greater than the electron donor tension component (γ^+), and the electron acceptor property dominates. And the van der Waals interaction energy is stronger than the acid-base interaction energy, and the van der Waals interaction energy is dominant. The cohesion free energy of the three pollutants was negative, indicating that the three pollutants showed attraction among themselves. From the size of the free energy value, it could be determined that the order of the strength of the action was FDP > MD > BSA. The cohesion free energy of the ternary system was −39.12 mJ·m^{-2}, which was lower than that of any single substance, indicating that the mixed pollutants weakened the interaction between solutes. According to the interfacial tension parameters of pollutants and the pristine membrane, the interfacial interaction energy at the minimum equilibrium distance (h_0 = 0.158 nm) can be calculated by substituting into Eqs. (12)–(14), and is shown in Table 11. The

Table 7
Mass transfer model fitting results R^2 for binary systems.

	CBM	SBM	IBM	CFM
UE010	**0.9506**	0.871	**0.9444**	**0.9375**
UE020	0.9016	**0.9874**	0.8904	0.8787
UE050	0.7683	**0.9803**	0.7515	0.7348
US020	0.8579	**0.8683**	0.8562	0.8544

Table 8
Mass transfer model fitting results R^2 for ternary systems.

	CBM	SBM	IBM	CFM
UE010	**0.9471**	0.8538	**0.9418**	**0.9349**
UE020	0.8576	**0.9271**	0.8433	0.8291
UE050	0.8602	**0.8934**	0.8567	0.8528
US020	0.1659	0.1931	0.1628	0.1597

Table 9
Characteristic parameters of feed solution and UE020.

	Zeta potential/mV	Contact angle/(°)		
		Pure water	Diiodomethane	Glycerol
FDP	−6.2 ± 1.70	76.68 ± 0.61	30.57 ± 0.08	68.45 ± 0.67
MD	−9.9 ± 2.75	71.49 ± 0.19	24.82 ± 0.26	59.04 ± 0.16
BSA	−7.7 ± 2.14	70.42 ± 0.23	32.52 ± 0.14	62.71 ± 0.20
Ternary	−4.6 ± 1.27	73.01 ± 0.76	30.50 ± 0.41	68.69 ± 0.25
UE020	−22.95 ± 0.50	78.31 ± 0.21	16.30 ± 0.37	68.71 ± 0.06

Table 10
Interfacial tension parameters and free energy of adhesion of pollutants (mJ·m^{-2}).

	γ^{LW}	γ^{+}	γ^{-}	γ^{AB}	γ^{TOT}	ΔG^{sis}
FDP	43.98	0.0033	7.81	0.32	44.31	−52.75
MD	46.22	0.1962	7.66	2.45	48.67	−51.12
BSA	43.15	0.0589	10.94	1.60	44.75	−40.72
Ternary	44.01	0.0568	11.69	1.63	45.64	−39.12
UE020	48.78	0.0691	6.12	1.30	50.08	−60.05

Table 11
Interfacial interaction energy at the minimum equilibrium distance (mJ·m^{-2}).

	$\Delta G^{AB}_{h_0}$	$\Delta G^{LW}_{h_0}$	$\Delta G^{EL}_{h_0}$	$\Delta G^{TOT}_{h_0}$
FDP	−47.32	−9.08	-6.81185×10^{-7}	−56.40
MD	−45.58	−9.85	-7.46344×10^{-7}	−55.43
BSA	−41.45	−8.79	-1.12726×10^{-6}	−50.23
Ternary	−40.41	−9.09	-1.21809×10^{-6}	−49.50

electrostatic double layer interaction energy is small and can be neglected. The results of the interfacial interaction energy at the minimum equilibrium distance are consistent with the adhesion interaction energy, demonstrating that the rate of formation of membrane fouling by various foulants on the UE020 is FDP > MD > BSA. Fig. 13 shows the trends of interaction energies of single component and ternary systems with UE020 at different separation distances. The formation of membrane fouling always starts from a shorter interaction distance, and the proximity interaction can describe the membrane fouling behavior more precisely [41]. Taking the ternary system as an example, the acid-base interaction energy is much larger than the van der Waals interaction energy in the range of 0.158–3.75 nm between the membrane and the pollutant, which is an important factor causing membrane fouling and plays a dominant role. The van der Waals interaction energy shows a long-range effect, which is consistent with the trend of the total interaction energy in the long-range range, *i.e.*, the van der Waals interaction energy dominates in the long-range range.

3.3. PAC as DM for fouling mitigation

Primary fouling mechanisms in the FDP/MD/BSA system involve CP by MD and BSA adsorption on membrane surfaces. To mitigate membrane fouling, PAC was deposited as an engineered barrier layer on pristine membrane surfaces (Fig. 14). This interlayer disrupts BSA-membrane interactions, thereby reducing specific filtration resistance despite PAC's inherent contribution to hydraulic resistance.

The PAC functional layer significantly changed the resistance distribution structure, with a reduction of 18.33% in total

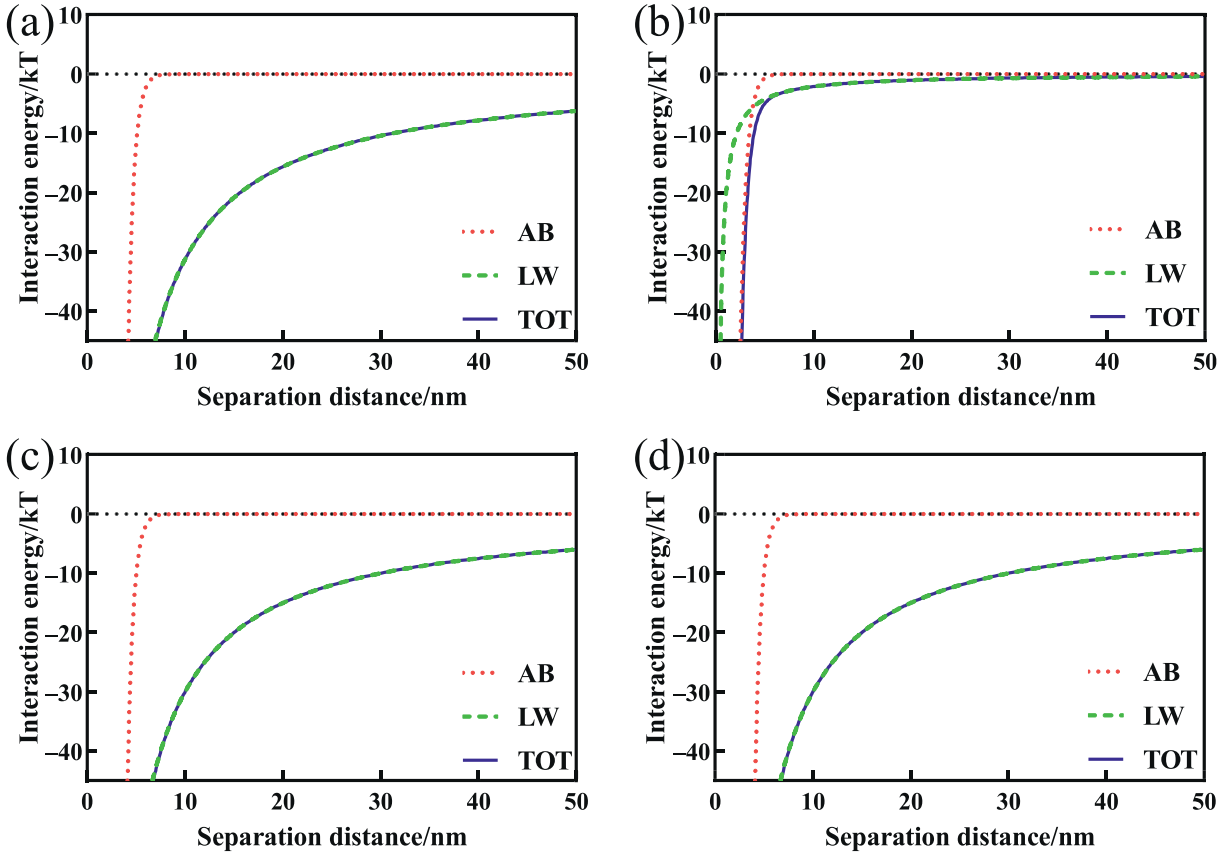

Fig. 13. Comparisons of interfacial interaction energies between different pollutants and UE020: (a) FDP, (b) MD, (c) BSA, (d) ternary system.

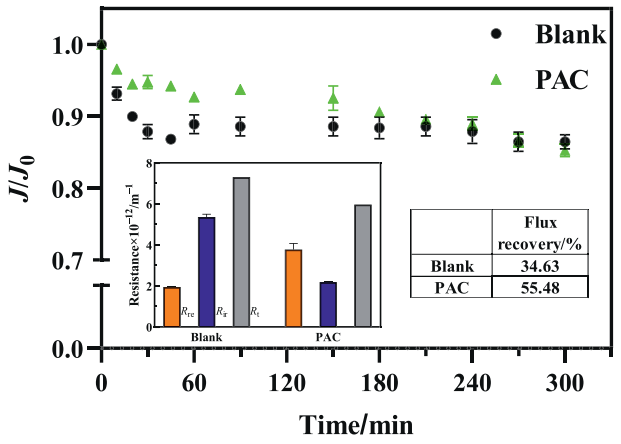

Fig. 14. PAC as a functional layer for fouling mitigation.

resistance and 59.14% in irreversible resistance. This indicated that the interaction between BSA and the membrane was significantly reduced, thereby improving BSA adsorption onto the membrane. Furthermore, reversible resistance increased by 93.84%, potentially due to PAC preventing BSA adsorption on the membrane surface and driving it into the boundary layer. This shift enhanced CP within the boundary layer. The flux recovery also increased by 20.85% due to the significant increase in the reversible resistance percentage. Although PAC addition requires its subsequent removal as an extraneous material during product recovery, its use during UF confers dual advantages. Since activated carbon is already necessary for post-treatment decolorization, integrating PAC at the UF stage simultaneously mitigates fouling and achieves preliminary decolorization, streamlining the process.

4. Conclusions

In the present study, a brief attempt was made to separate the simulated solution of FDP multi-enzyme system by UF. All four of the membranes selected were found to have some degree of separation effect, and the fouling behavior of the separation process was explored in depth, and the following conclusions were obtained.

1) In the ternary system, the retention rate of UE020 on BSA could reach 99.97%, and $\alpha_{(FDP/MD)}$ reached 7.41, the yield of FDP was 93.63%, which realized the high efficiency of separation of the target product FDP from BSA and MD.
2) It was found by analyzing the single component fouling process: the fouling formed by FDP was mainly intra-pore adsorption, narrowing the pore size, but contributes the least to the total system resistance; MD mainly formed CP and then increased the filtration resistance, which was the key factor constituting the total resistance; BSA adsorbed on the membrane surface to form an irreversible resistance.
3) Analysis of the UF process by series resistance model and Hermia model found that: CP is the main factor constituting resistance in FDP/MD system (>60%), and the addition of BSA increases the irreversible resistance (>40%). MD enrichment in the boundary layer contributes to increased CP, whereas BSA adsorption occurs directly on the membrane surface. FDP enters the pore and adsorbs on the pore wall, so that the average pore size of the membrane also decreases from 5.89 nm to 2.69 nm. Both the polar and van der Waals interaction energies between the foulant and the membrane showed attraction effect, and the total interfacial energy showed attraction in the full range of distance.
4) The addition of PAC as a functional layer significantly changed the resistance distribution structure, reducing the irreversible resistance by 59.14% and the total resistance by 18.33%.

Fouling mechanism analysis demonstrated that CP remains the predominant flux-limiting factor, with PAC-derived functional layer showing limited efficacy in CP mitigation (total resistance reduction <20%). Notably, the PAC-mediated interface primarily translocated resistance components from the membrane surface to the boundary layer, resulting in marginal flux improvement. Future research should integrate colloidal interaction modeling with mass transfer simulations to decode the functional layer-pollutant flux nexus.

CRediT Authorship Contribution Statement

Zhengxin Mao: Writing – review & editing, Writing – original draft, Data curation, Conceptualization. Jiachang Shen: Writing – review & editing. Mengxin Liu: Writing – review & editing. Yanjie Ji: Writing – review & editing. Qinhong Wang: Writing – review & editing. Maohua Yang: Writing – review & editing, Supervision, Project administration. Jianmin Xing: Writing – review & editing, Supervision, Project administration.

Data Availability

Data will be made available on request.

Declaration of Competing Interest

The authors declare that they have no known competing financial interests or personal relationships that could have appeared to influence the work reported in this paper.

Acknowledgements

This work acknowledges the funding support provided by the Strategic Priority Research Program of the Chinese Academy of Sciences (XDC0120402) and the National Key Research & Development Program of China (2022YFC2105103).

References

[1] Z.G. Movahed, R. Yarani, P. Mohammadi, K. Mansouri, Sustained oxidative stress instigates differentiation of cancer stem cells into tumor endothelial cells: pentose phosphate pathway, reactive oxygen species and autophagy crosstalk, *Biomed. Pharmacother.* 139 (2021) 111643.
[2] S. Supper, N. Anton, J. Boisclair, N. Seidel, M. Riemenschnitter, C. Curdy, T. Vandamme, Chitosan/glucose 1-phosphate as new stable *in situ* forming depot system for controlled drug delivery, *Eur. J. Pharm. Biopharm.* 88 (2) (2014) 361–373.
[3] K. Bensaad, A. Tsuruta, M.A. Selak, M.N.C. Vidal, K. Nakano, R. Bartrons, E. Gottlieb, K.H. Vousden, TIGAR, a p53-inducible regulator of glycolysis and apoptosis, *Cell* 126 (1) (2006) 107–120.
[4] J.F. Shi, Y.Z. Wu, S.H. Zhang, Y. Tian, D. Yang, Z.Y. Jiang, Bioinspired construction of multi-enzyme catalytic systems, *Chem. Soc. Rev.* 47 (12) (2018) 4295–4313.
[5] J.G. Yang, T. Zhang, C.Y. Tian, Y.M. Zhu, Y. Zeng, Y. Men, P. Chen, Y.X. Sun, Y.H. Ma, Multi-enzyme systems and recombinant cells for synthesis of valuable saccharides: advances and perspectives, *Biotechnol. Adv.* 37 (7) (2019) 107406.
[6] T. Cai, H.B. Sun, J. Qiao, L.L. Zhu, F. Zhang, J. Zhang, Z.J. Tang, X.L. Wei, J.G. Yang, Q.Q. Yuan, W.Y. Wang, X. Yang, H.Y. Chu, Q. Wang, C. You, H.W. Ma, Y. X. Sun, Y. Li, C. Li, H.F. Jiang, Q.H. Wang, Y.H. Ma, Cell-free chemoenzymatic starch synthesis from carbon dioxide, *Science* 373 (6562) (2021) 1523–1527.
[7] C.Y. Tian, J.G. Yang, C. Liu, P. Chen, T. Zhang, Y. Men, H.W. Ma, Y.X. Sun, Y.H. Ma, Engineering substrate specificity of HAD phosphatases and multienzyme systems development for the thermodynamic-driven manufacturing sugars, *Nat. Commun.* 13 (1) (2022) 3582.

[8] W. Wang, M.X. Liu, C. You, Z.M. Li, Y.P. Zhang, ATP-free biosynthesis of a high-energy phosphate metabolite fructose 1,6-diphosphate by *in vitro* metabolic engineering, *Metab. Eng.* 42 (2017) 168–174.
[9] D.J. Wichelecki, M.W. Vetting, L. Chou, N. Al-Obaidi, J.T. Bouvier, S.C. Almo, J. A. Gerlt, ATP-binding cassette (abc) transport system solute-binding protein-guided identification of novel d-Altritol and galactitol catabolic pathways in agrobacterium tumefaciens C58, *J. Biol. Chem.* 290 (48) (2015) 28963–28976.
[10] Y.J. Li, T. Shi, P.P. Han, C. You, Thermodynamics-driven production of value-added d-allulose from inexpensive starch by an *in vitro* enzymatic synthetic biosystem, *ACS Catal.* 11 (9) (2021) 5088–5099.
[11] J.C. Shen, M.H. Yang, J.M. Xing, Efficient separation of HEPES and CO_2-derived fructose by nanofiltration: optimizing pH for improved separation and proposing a potential mechanism, *Sep. Purif. Technol.* 355 (2025) 129657.
[12] X. Wen, Y.H. Ning, H.B. Lin, Y.L. Ren, C. Li, Y.J. Liu, C.J. Zhang, J.Q. Lin, J.Q. Lin, D-Allulose (d-psicose) biotransformation from d-glucose, separation by simulated moving bed chromatography (SMBC) and purification by crystallization, *Process. Biochem.* 119 (2022) 29–38.
[13] C. Nobre, P. Suvarov, G. De Weireld, Evaluation of commercial resins for fructo-oligosaccharide separation, *Nat. Biotechnol.* 31 (1) (2014) 55–63.
[14] Y. Shi, X.Z. Kong, C.M. Zhang, Y.M. Chen, Y.F. Hua, Adsorption of soy isoflavones by activated carbon: kinetics, thermodynamics and influence of soy oligosaccharides, *Chem. Eng. J.* 215-216 (2013) 113–121.
[15] J.Q. Luo, B. Zeuner, S.T. Morthensen, A.S. Meyer, M. Pinelo, Separation of phenolic acids from monosaccharides by low-pressure nanofiltration integrated with laccase pre-treatments, *J. Membr. Sci.* 482 (2015) 83–91.
[16] S. Novalin, T. Kongbangkerd, M. Reisinger, S. Pruksasri, Integration of electrodialysis into an enzymatic synthesis for the separation of phosphate from glucose-1-phosphate, *Sep. Purif. Technol.* 182 (2017) 224–229.
[17] C. Compagno, A. Tura, B.M. Ranzi, E. Martegani, Bioconversion of lactose/whey to fructose diphosphate with recombinant saccharomyces cerevisiae cells, *Biotechnol. Bioeng.* 42 (3) (1993) 398–400.
[18] M. Haribabu, D.E. Dunstan, G.J.O. Martin, M.R. Davidson, D.J.E. Harvie, Simulating the ultrafiltration of whey proteins isolate using a mixture model, *J. Membr. Sci.* 613 (2020) 118388.
[19] Z.L. Jia, F.Z. Li, X. Zhang, X. Zhao, Effects of cation exchange membrane properties on the separation of salt from high-salt organic wastewater by electrodialysis, *Chem. Eng. J.* 475 (2023) 146287.
[20] H. Wang, R. Ding, T. Wu, X.J. Zhang, L.J. Cheng, K. Xu, Y. Zheng, X. Pang, G.L. Ji, L.Q. Shen, J.J. Li, R.N. Zhang, Z.Y. Jiang, Ionic covalent organic framework engineered super-charged thin-film composite polyamide membrane for desalination, *Chem. Eng. J.* 510 (2025) 161671.
[21] K.F. Chen, S.L. Hao, H. Lyu, G. Luo, S.C. Zhang, J.M. Chen, Ion exchange separation for recovery of monosaccharides, organic acids and phenolic compounds from hydrolysates of lignocellulosic biomass, *Sep. Purif. Technol.* 172 (2017) 100–106.
[22] R.R. Chang, L. Xiong, M. Li, J. Liu, Y.F. Wang, H.H. Chen, Q.J. Sun, Fractionation of debranched starch with different molecular weights *via* edible alcohol precipitation, *Food Hydrocoll.* 83 (2018) 430–437.
[23] W.L. Yang, F. Zhou, J. Lee, J. Kim, D.Y. Kwon, Y. Kim, H.Q. Ren, S. Hong, M. Zhan, B. Wu, Understanding the fouling characteristics in ultrafiltration membrane for marine algae-laden seawater pretreatment: focus on the role of algal extracellular organic matter, *J. Clean. Prod.* 479 (2024) 144084.
[24] D.C. Lin, L.M. Bai, D.L. Xu, H.R. Wang, H. Zhang, G.B. Li, H. Liang, Nanofiltration scaling influenced by coexisting pollutants considering the interaction between ferric coagulant and natural organic macromolecules, *Chem. Eng. J.* 413 (2021) 127403.
[25] J. Jawad, A.H. Hawari, S. Javaid Zaidi, Artificial neural network modeling of wastewater treatment and desalination using membrane processes: a review, *Chem. Eng. J.* 419 (2021) 129540.
[26] S.Z. Hao, X.H. Zhao, H.W. Zhang, Y. Wu, C. Fang, X.J. Wang, Effects of a novel bimetallic catalytic biofilter-based pretreatment technique on the form of ultrafiltration membrane fouling, *Chin. J. Chem. Eng.* 28 (10) (2020) 2513–2522.
[27] S. Jeong, Y.H. Jeong, B. Gu, S. Jeong, Comparative study of anti-scaling performance in membrane distillation: membrane spacer *vs*. patterned module *vs*. patterned membrane, *Chem. Eng. J.* 493 (2024) 152470.
[28] J. Hermia, Constant pressure blocking filtration laws - application to power-law non-Newtonian fluids, *Trans. Inst. Chem. Eng.* 60 (1982) 183–187.
[29] Y.C. Sun, X. Yang, Z.Y. Zhang, Q.G. Zhang, D. Xia, Q.B. Li, Y.P. Wang, Configuration of multi-stage membrane process towards effective separation of C, N and P from real-life biogas slurry: design, optimization and analysis, *Chem. Eng. Sci.* 303 (2025) 120970.
[30] M.M. Bradford, A rapid and sensitive method for the quantitation of microgram quantities of protein utilizing the principle of protein-dye binding, *Anal. Biochem.* 72 (1–2) (1976) 248–254.
[31] X.W. Zhu, Z.Y. Sun, F.X. Tan, F.Y. Chen, X.S. Luo, F.H. Wang, D.J. Wu, H. Liang, D.L. Xu, X.X. Cheng, Tailoring high-performance polyester loose nanofiltration membrane for selective separation of salt/dyes: the equilibrium of condensation and hydrolysis, *Sep. Purif. Technol.* 333 (2024) 125848.
[32] X.W. Zhu, X.Y. Zhang, J.Y. Li, X.S. Luo, D.L. Xu, D.J. Wu, W.Q. Wang, X.X. Cheng, G.B. Li, H. Liang, Crumple-textured polyamide membranes *via* MXene nanosheet-regulated interfacial polymerization for enhanced nanofiltration performance, *J. Membr. Sci.* 635 (2021) 119536.
[33] R.W. Field, D. Wu, J.A. Howell, B.B. Gupta, Critical flux concept for microfiltration fouling, *J. Membr. Sci.* 100 (3) (1995) 259–272.
[34] N. Wemsy Diagne, M. Rabiller-Baudry, L. Paugam, On the actual cleanability of polyethersulfone membrane fouled by proteins at critical or limiting flux, *J. Membr. Sci.* 425-426 (2013) 40–47.
[35] S.L. Liu, C. Rouquié, M. Frappart, A. Szymczyk, M. Rabiller-Baudry, E. Couallier, Separation of lipids and proteins from clarified microalgae lysate: the effect of lipid-protein interaction on the cross-flow and shear-enhanced microfiltration performances, *Sep. Purif. Technol.* 328 (2024) 124985.
[36] R.Y. Wang, S.H. Lin, Pore model for nanofiltration: history, theoretical framework, key predictions, limitations, and prospects, *J. Membr. Sci.* 620 (2021) 118809.
[37] L. Vargas-Campos, J. de Dios Figueroa-Cárdenas, D. Tochihuitl-Vázquez, R. Ramírez-Bon, J.M. Yáñez-Limón, J.F. Pérez-Robles, Study of the dextrose equivalent of maltodextrins in electrospinning using an ethanol/water mixture as the electrospinning solvent, *Food Hydrocoll.* 139 (2023) 108498.
[38] H. Xu, C. Yao, J. Ma, A. Wang, Y. Li, M.M. Ding, Mechanism of sodium alginate (SA) fouling with the co-existing cations in membrane distillation process, *Desalination* 605 (2025) 118728.
[39] E. Arkhangelsky, A. Bazarbayeva, A. Kamal, J. Kim, V. Inglezakis, V. Gitis, Tangential streaming potential, transmembrane flux, and chemical cleaning of ultrafiltration membranes, *Sep. Purif. Technol.* 258 (2021) 118045.
[40] H. Choi, K. Zhang, D.D. Dionysiou, D.B. Oerther, G.A. Sorial, Effect of permeate flux and tangential flow on membrane fouling for wastewater treatment, *Sep. Purif. Technol.* 45 (1) (2005) 68–78.
[41] Y.H. Chen, R. Zhang, G.X. Wu, J.P. Li, Y.S. Ren, X.X. Duan, Thermodynamic mechanism insights into the dynamic evolution of nanofiltration membrane fouling: effect of calcium ion on organic fouling, *Desalination* 568 (2023) 117036.